Supplementary Information

High Selectivity of CO_2 Hydrogenation to CO by Controlling the Valence State of Nickel using Perovskite

Baohuai Zhao,‡[ab] Binhang Yan,‡[bc] Zhao Jiang,[e] Siyu Yao,[b] Zongyuan Liu,[b] Qiyuan Wu,[d] Rui Ran,*[a] Sanjaya D. Senanayake,[b] Duan Weng[a] and Jingguang. G. Chen*[e]

[a] School of Materials Science and Engineering, Tsinghua University, Beijing, 100084, China

[b] Chemistry Department, Brookhaven National Laboratory, Upton, New York 11973, United States

[c] Department of Chemical Engineering, Tsinghua University, Beijing, 100084, China

[d] Department of Material Science and Chemical Engineering, Stony Brook University, Stony Brook, New York 11794, United States

[e] Department of Chemical Engineering, Columbia University, New York, New York 10027, United States

‡ These authors contributed equally.

*E-mail: ranr@tsinghua.edu.cn.

*E-mail: jgchen@columbia.edu.

Table of Contents

1. Catalyst synthesis

The perovskites, $LaFe_{1-x}Ni_xO_3$ (x = 0, 0.1, 0.3, 0.5, and 1), were prepared by a citrate method which was similar to the process in literature,[1] using $La(NO_3)_3 \cdot 6H_2O$ (99.9%, Alfa Aesar), $Fe(NO_3)_3 \cdot 9H_2O$ (99.99%, Sigma-Aldrich), $Ni(NO_3)_2 \cdot 6H_2O$ (99.999%, Sigma-Aldrich) and citric acid (99+%, Alfa Aesar). The stoichiometric nitrates were dissolved in deionized water. Then 10% excess citric acid over the number of ionic equivalents of cations was added to the aqueous solution. The resulting solution was stirred and evaporated at 363 K until the formation of a gel. The gel was dried in an oven at 383 K overnight, forming a spongy amorphous citrate precursor. The precursor was milled and calcined in air at 573 K for 1 h to decompose the organics, then heated to 1023 K at 1 K min^{-1} and held for 5 h to obtain the perovskite structure.

2. BET

The Brunauer-Emmett-Teller (BET) specific areas were determined based on N_2 adsorption isotherms recorded at 77 K using an AMI-300ip (Altamira) instrument equipped with a thermal conductivity detector (TCD). Prior to the N_2 adsorption, the catalysts were outgassed at 383 K under He flow for 30 min to desorb moisture and other gas molecules adsorbed on the surfaces and inside the porous networks. The BET specific surface area of $LaNiO_3$, $LaFe_{0.5}Ni_{0.1}O_3$, and $LaFeO_3$ are 8.7, 9.0, and 10.8 m^2 g^{-1}, respectively.

3. Catalytic performance

Reactions of CO_2 and H_2 were performed in a quartz tube reactor (inner diameter 1/4 in.) under atmospheric pressure. Approximately 100 mg of the catalysts, sieved to 40–60 mesh, were used for steady-state experiments. With the constant total flow rate of 40 mL min^{-1}, CO_2, H_2, and Ar as a diluent were introduced at 1:2:5 ratio, respectively, into the reactor. The catalysts were heated to 673 K and kept at this temperature for 14 h for stability measurements. Then the temperature was ramped down to lower temperatures with an interval of 10 K to evaluate the activity at different temperatures. For the activity test of $LaNiO_3$, another experiment was performed with 15 mg

catalyst and 85 mg silica (40–60 mesh) inorder to control the CO_2 conversion. The testing condition was same to the process above. The gas products were analyzed on-line using a gas chromatography (GC, Agilent 7890B), equipped with a flame ionization detector (FID) and a thermal conductivity detector (TCD). Control experiments were performed using a blank reactor and 100 mg quartz sand at 673 K. Both cases showed little activity, indicating that the gas-phase reaction and quartz sand will not strongly affect the reaction.

The steady-state conversion (*X*), turnover frequency (*TOF*), yield (*Y*), and selectivity (*S)* are defined as:

$$X_{\text{reactant}} = \frac{F_{\text{reactant}}^{\text{inlet}} - F_{\text{reactant}}^{\text{outlet}}}{F_{\text{reactant}}^{\text{inlet}}} \times 100\% \quad (1)$$

$$TOF_{\text{reactant}} = \frac{F_{\text{reactant}}^{\text{inlet}} \times X}{U_{\text{Ni}} \times W_{\text{catalyst}}} \times 100\% \text{ , (mol mol}_{\text{Ni}}^{-1}\text{ min}^{-1}\text{)} \quad (2)$$

$$Y_{\text{CO or CH}_4} = \frac{F_{\text{CO or CH}_4}^{\text{outlet}}}{F_{\text{CO}_2}^{\text{inlet}}} \times 100\% \quad (3)$$

$$S_{\text{CO or CH}_4} = \frac{Y_{\text{CO or CH}_4}}{X_{\text{CO}_2}} \times 100\% \quad (4)$$

where, *F* is the flow rate of reactant, mol min^{-1}; U_{Ni} is the loading amount of nickel, mol g^{-1}; *W* is the weight of catalyst used, g.

Fig. S1 presents the catalytic performance of CO_2 conversion, H_2 conversion, CO yield, and CH_4 yield achieved by $LaNiO_3$, $LaFe_{0.5}Ni_{0.5}O_3$, and $LaFeO_3$ at different temperatures from 613 to 673 K. As shown in Fig. S1a and b, the CO_2 conversion and H_2 conversion over the three catalysts take the same trend, which is $LaNiO_3$ > $LaFe_{0.5}Ni_{0.5}O_3$ > $LaFeO_3$. For the reaction at 673 K over 14 h (Fig. S2), $LaNiO_3$ has the highest CO_2 conversion and H_2 conversion all the time, followed by $LaFe_{0.5}Ni_{0.5}O_3$ while the activity of $LaFeO_3$ is still very poor. $LaNiO_3$ shows the stable conversion of CO_2 and H_2, as well as the yield of products (CH_4 and CO). For

$LaFe_{0.5}Ni_{0.5}O_3$, the CO_2 and H_2 conversion decrease by 9.1% and 14.8%, respectively. The CO yield of $LaFe_{0.5}Ni_{0.5}O_3$, drops from 18.3% to 15.7%, while the CH_4 yield drops from 6.9% to 0.5%, respectively. Table S1 summarizes the catalytic performance of the catalysts by averaging data points in 12–14 h on stream, in which the results of the $LaFe_{0.9}Ni_{0.1}O_3$ and $LaFe_{0.7}Ni_{0.3}O_3$ catalysts are also included. The Fe-containing catalysts show ~100% CO selectivity at 673 K. These catalysts also have high CO selectivity (> 94%) at the other temperature points in the range of 613–673 K.

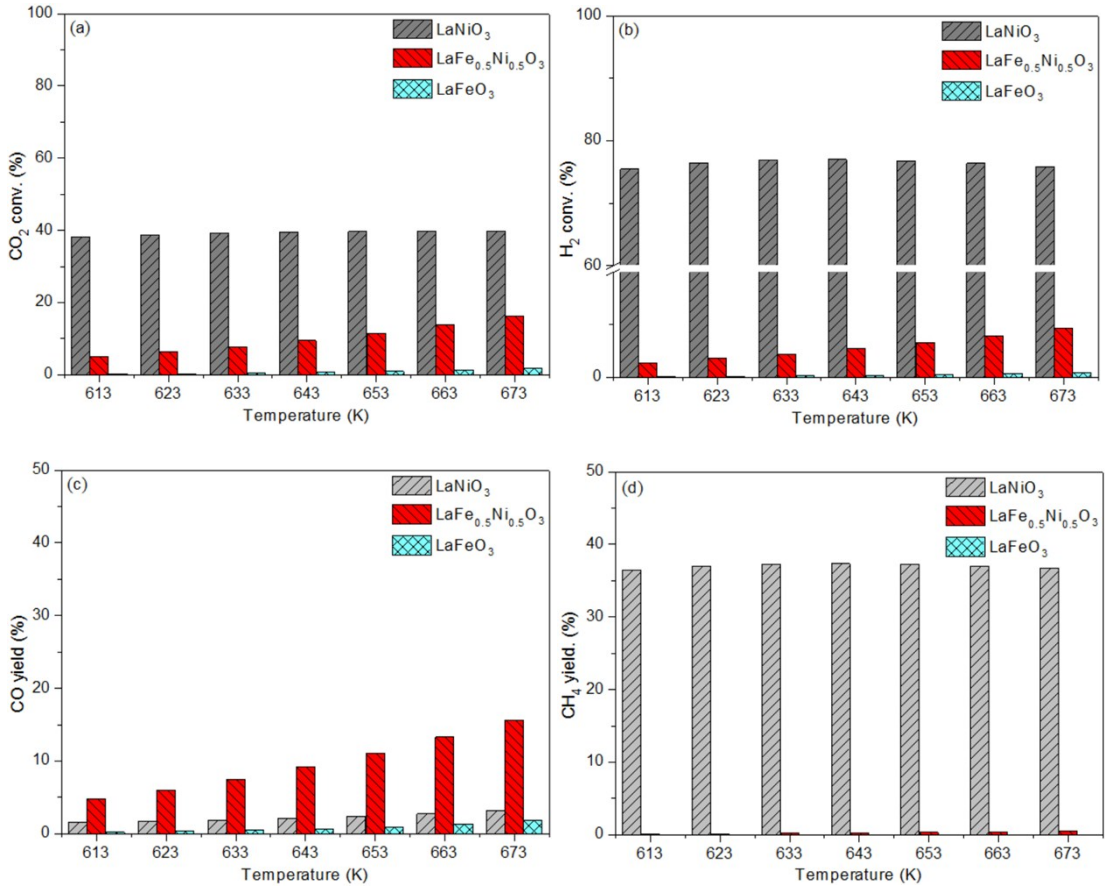

Fig. S1 The (a) CO_2 conversion, (b) H_2 conversion, (c) CO yield, and (d) CH_4 yield over the $LaNiO_3$, $LaFe_{0.5}Ni_{0.5}O_3$, and $LaFeO_3$ catalysts at different temperatures (Reaction conditions: $CO_2/H_2/Ar$ = 5/10/25 ml, GHSV = 24,000 mL h^{-1} $g_{cat.}^{-1}$, 1 atm).

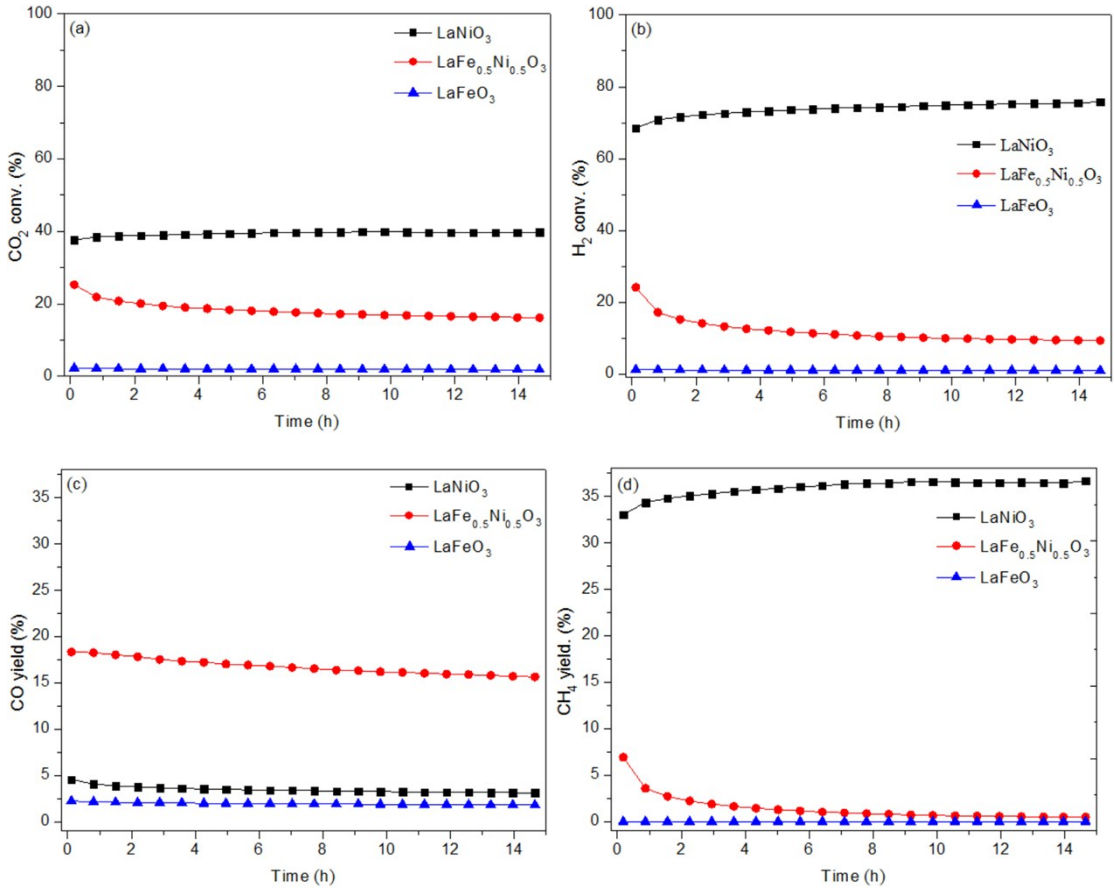

Fig. S2 The (a) CO_2 conversion, (b) H_2 conversion, (c) CO yield, and (d) CH_4 yield over the $LaNiO_3$, $LaFe_{0.5}Ni_{0.5}O_3$, and $LaFeO_3$ catalysts during the stability measurements (Reaction conditions: $CO_2/H_2/Ar$ = 5/10/25 ml, GHSV = 24,000 mL h^{-1} $g_{cat.}^{-1}$, 1 atm, 673 K).

Table S1. The catalytic performance of the perovskite catalysts with different Fe/Ni ratios.

Sample	CO_2 conversion (%)	H_2 conversion (%)	CH_4 yield (%)	CO yield (%)	CH_4 selectivity (%)	CO selectivity (%)
$LaFeO_3$	1.8	1.0	0.0	1.8	0.0	100.0
$LaFe_{0.9}Ni_{0.1}O_3$	5.3	2.7	0.0	5.3	0.0	100.0
$LaFe_{0.7}Ni_{0.3}O_3$	10.2	5.6	0.2	10.0	1.9	98.0
$LaFe_{0.5}Ni_{0.5}O_3$	16.3	11.4	0.5	15.8	3.2	96.6
$LaNiO_3$	39.7	75.5	36.5	3.2	92.0	8.0

Reaction conditions: 100 mg catalyst, 673 K, calculated by averaging data points in 12–14 h on stream, $CO_2/H_2/Ar$ = 5/10/25 mL min^{-1}.

4. TEM

The morphologies and particle size distributions of the fresh and spent catalysts were analyzed using transmission electron microscopy (TEM; JEM-2100, JEOL) at an accelerating voltage of 200 kV. Specimens for TEM were prepared by dispersing the samples ultrasonically in ethanol for 15 min. After dispersion, a droplet was deposited on a perforated carbon film supported by a copper grid and allowed to dry. The TEM images of the fresh $LaNiO_3$ and $LaFe_{0.5}Ni_{0.5}O_3$ catalysts are shown in Fig. S3. Both catalysts take a morphology of severely sintered particles. The edges of the particles are very clear without any other smaller particles as can be seen in the magnified images in Fig. S3b and d for $LaNiO_3$ and $LaFe_{0.5}Ni_{0.5}O_3$, respectively.

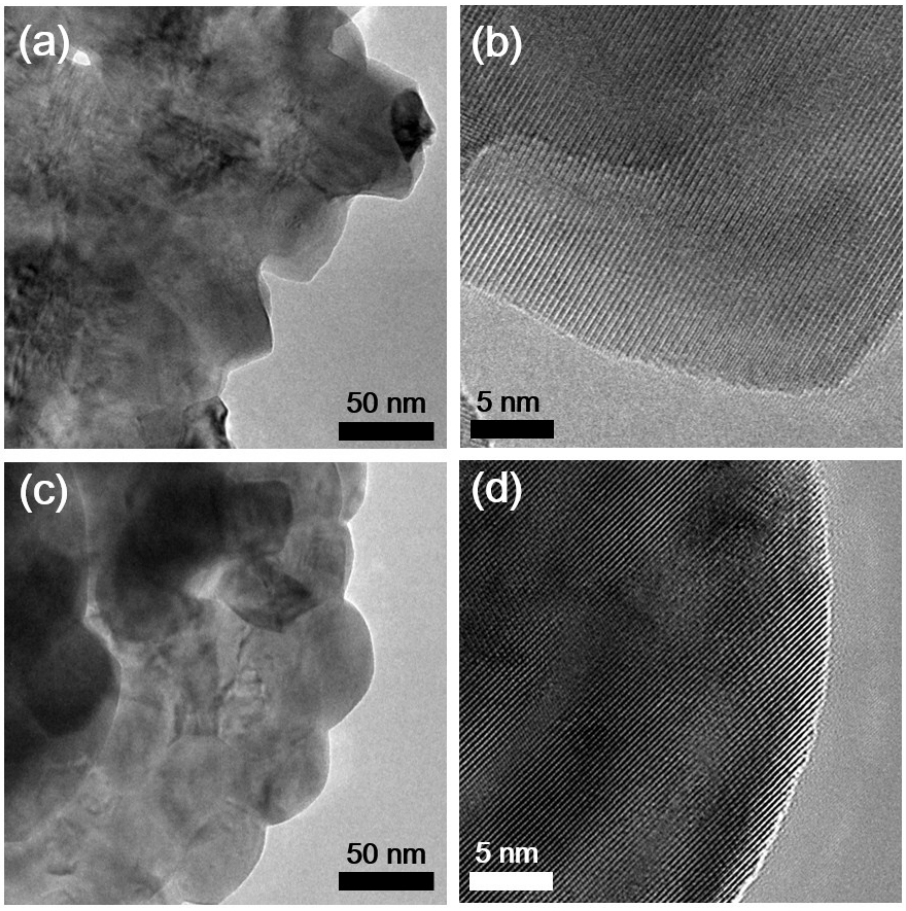

Fig. S3 TEM images of the fresh catalysts (a) and (b) $LaNiO_3$; (c) and (d) $LaFe_{0.5}Ni_{0.5}O_3$.

5. XRD

The *ex-situ* and *in-situ* high-resolution synchrotron X-ray diffraction (XRD) patterns were collected at beamline 17-BM with a wavelength of 0.24128 Å at the advanced photon source (APS) at Argonne National Lab (ANL). For the *ex-situ* experiments,

the samples were loaded into a polyimide tubing (inner diameter 0.9 mm). For the *in-situ* experiments, an amorphous silica capillary (inner diameter 0.9 mm) with samples inside was mounted to a flow cell setup, as described in detail in previous work.[2, 3] During the measurement, a gaseous mixture of CO_2, H_2, and He with a volume ratio of 1/2/2 was passed through the capillary at a total flow rate of 10 mL min^{-1}. The temperature was increased from 300 to 673 K at a rate of 20 K min^{-1} and then held at 673 K for 40 min. After that, the CO_2 was cut off to leave H_2 (4.0 mL min^{-1}) and He (6.0 mL min^{-1}) in the gas flow for 30 min. Finally, the temperature was cooled down to room temperature. The XRD patterns were recorded all the time during in each process.

The *ex-situ* XRD patterns of the fresh and spent samples of $LaNiO_3$, $LaFe_{0.5}Ni_{0.5}O_3$, and $LaFeO_3$ are presented in Fig. S4a. The three fresh samples of $LaNiO_3$, $LaFe_{0.5}Ni_{0.5}O_3$, and $LaFeO_3$ all display structures of perovskites.[4-6] In the perovskite structure, the Fe and Ni ions are connected with oxygen atoms to form the MO_6 (M = Fe or Ni) octahedra. The Fe and Ni ions in this form are regarded with the valence state of 3+.[5, 7] The diffraction patterns of the $LaFe_{0.5}Ni_{0.5}O_3$-spent and $LaFeO_3$-spent are also assigned to perovskite structures while the phase structure of $LaNiO_3$-spent is changed to $LaNiO_{2.5}$.[8] Fig. S4b shows the positions of the strongest diffraction peaks around $2\theta = 5.0°$ of the samples. The peak of $LaFe_{0.5}Ni_{0.5}O_3$-fresh is located between those of the $LaFeO_3$-fresh and $LaNiO_3$-fresh, due to the smaller radius of Ni^{3+} (0.56 Å) than Fe^{3+} (0.65 Å).[9, 10] After the reaction test, the peak position of the $LaFeO_3$-spent keeps almost the same to the fresh one. The peak of $LaFe_{0.5}Ni_{0.5}O_3$-spent shifts to a lower angle due to the lattice expansion resulted from the exclusion of Ni^{3+} ions from the lattice and the formation of oxygen vacancies.[9] For the *in-situ* measurements at 673 K under different atmospheres (CO_2+H_2+He or H_2+He), the XRD patterns of the two catalysts in Fig. S5 are without any further change, indicating that their main structures can be maintained under such conditions.

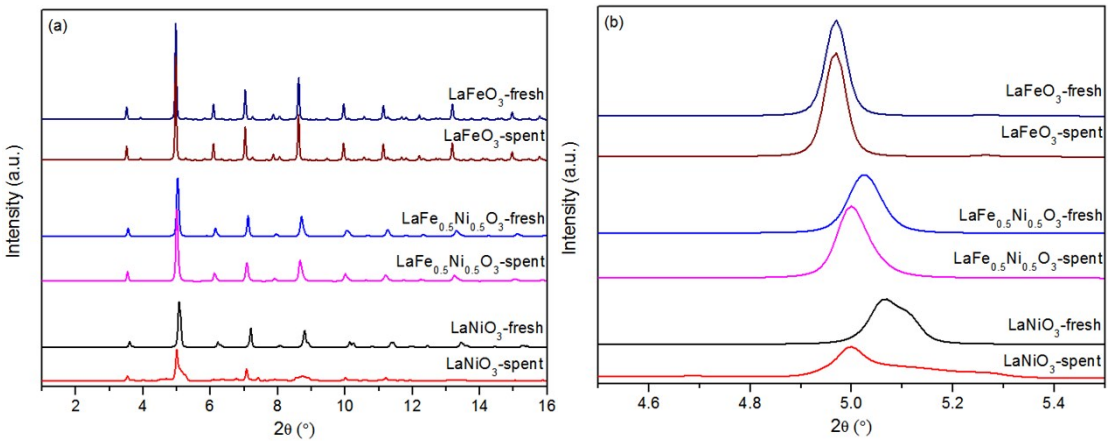

Fig. S4 XRD patterns of the fresh and spent catalysts of $LaNiO_3$, $LaFe_{0.5}Ni_{0.5}O_3$, and $LaFeO_3$.

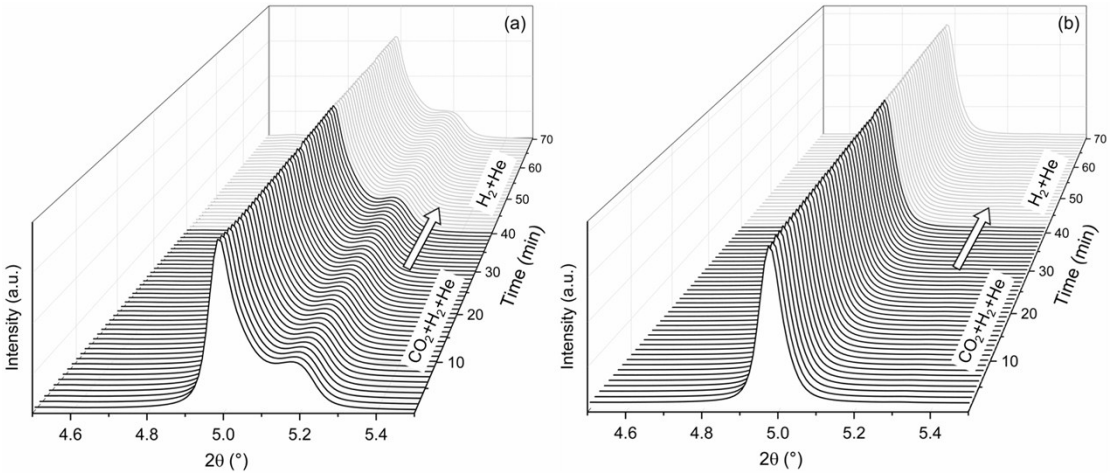

Fig. S5 *In-situ* XRD patterns of (a) $LaNiO_3$ and (b) $LaFe_{0.5}Ni_{0.5}O_3$ at 673 K in different atmosphere.

6. H_2-TPR

H_2 temperature-programmed reduction (TPR) experiments were carried out on the AMI-300ip (Altamira) instrument to examine the variations in the reducibility of the perovskite catalysts. For each TPR experiment, approximately 50 mg of the fresh catalyst was put into a U-shaped quartz tube and pre-treated at 573 K for 30 min in 10% O_2/He flow (50 mL min^{-1}) and then cooled to 300 K. The flow was then switched to a gas mixture of 10% H_2/Ar with a constant flow rate of 50 mL min^{-1}, and the TPR measurements were performed with a heating rate of 10 K min^{-1} to 1273 K. The amount of hydrogen consumed as a function of reduction temperature was continuously recorded by TCD, which could be used to compare the reducibility of

the catalysts.

The reduction curves of the catalysts are shown in Fig. S6. For $LaNiO_3$, the reduction proceeds with a sequence of Ni^{3+} to Ni^{2+} and Ni^{2+} to metallic Ni.[11-14] The multiple reduction peaks are overlapping with each other in the lower temperature range (300–673 K) and higher temperature range (673–800 K), and $LaNiO_{2.5}$ and La_2NiO_4 are generally regarded as the intermediates.[11-14] The reduction curve of $LaFeO_3$ displays a wide reduction peak starting from 920 K, which could be assigned to the reduction of Fe^{3+}.[14] This demonstrates that the pure $LaFeO_3$ perovskite is rather stable until 920 K. According to the literature [15, 16], the reduction peak ranging from 406 to 580 K in $LaFe_{0.5}Ni_{0.5}O_3$ is ascribed to the reduction of Ni^{3+} to Ni^{2+} and that located in the higher temperature range (> 700 K) is assigned to the reduction of Ni and Fe ions to their metallic state. In the case of $LaNiO_3$, the Ni ions are totally reduced to the metallic state before 800 K. However, the H_2 consumption of $LaFe_{0.5}Ni_{0.5}O_3$ before 800 K takes 24.5% of the total amount. If all the Ni ions in this sample were reduced to the metallic state before 800 K, this ratio should be greater than 50%, suggesting that the $LaFe_{0.5}Ni_{0.5}O_3$ perovskite is able to stabilize the oxidized states of Ni species to a higher temperature range than $LaNiO_3$.

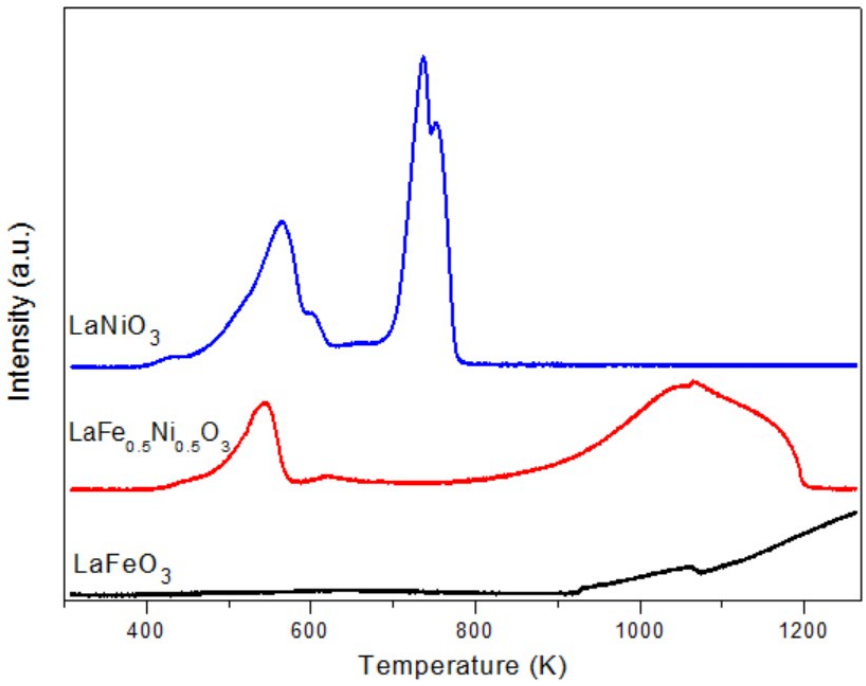

Fig. S6 TPR profiles of the fresh $LaNiO_3$, $LaFe_{0.5}Ni_{0.5}O_3$, and $LaFeO_3$ catalysts.

7. X-ray absorption near-edge structure (XANES)

The *in-situ* XANES spectra of Ni K-edge (8333 eV) were collected at beamline 2-2 of the Stanford Synchrotron Radiation Lightsource (SSRL) in fluorescence mode. About 50 mg catalyst (60–80 mesh) was loaded into a 3 mm o.d. glassy-carbon tube, packed with quartz wool on both sides of the sample. A reaction gas mixture of CO_2, H_2, and He with a ratio of 1/2/2 (10 mL min^{-1} in total) was introduced into the reactor. After the spectra being collected at 300 K (fresh state), the reactor was heated to 673 K with a ramping rate of 20 K min^{-1} and hold for 40 min. Then the gas was switched to a reducing atmosphere with H_2 (4 mL min^{-1}) and He (6 mL min^{-1}) for 30 min. After that, the reactor was cooled down to 300 K. The spectra were also collected at the reaction and reducing conditions. All of the XANES spectra were taken for three scans. To quantify the fraction of Ni-related species of each sample at the reaction and reducing conditions, the spectra were fitted using the linear combination function in Athena (IFEFFIT 1.2.11 data analysis package). The spectra of Ni foil (Ni^0), NiO (Ni^{2+}), and the fresh sample (Ni^{3+}) were employed as references for the fitting. The Ni/ZrO_2 catalyst in Fig. S7 is used as a control sample, which is prepared by impregnation method and calcined at 450 °C for 5 h.

Table S2: The linear combination fitting results of Ni K-edge

Catalyst	Treatment condition	Ni^{3+} [a]	Ni^{2+} [b]	Ni^0 [c]
$LaNiO_3$	Reaction	33±1%	56±2%	11±2%
	H_2 reduced	19±1%	40±1%	41±1%
$LaFe_{0.5}Ni_{0.5}O_3$	Reaction	36±1%	64±1%	0±1%
	H_2 reduced	34±1%	67±1%	0±2%

[a] fresh sample. [b] NiO. [c] Ni foil.

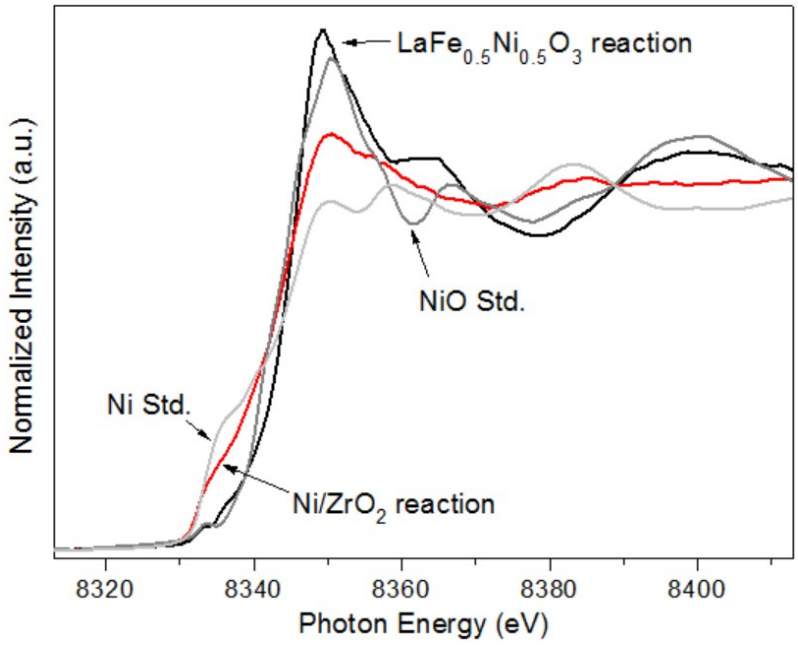

Fig. S7 The *in-situ* Ni K-edge XANES of the 1.5 wt% Ni/ZrO_2 and $LaFe_{0.5}Ni_{0.5}O_3$ catalysts in the reaction condition.

8. XPS

In-situ AP-XPS measurements were performed on a system (SPECS Surface Nano Analysis GmbH, Germany) equipped with Al Kα radiation (hν = 1486.6 eV) to identify the chemical states of surface Ni species. The powder samples were pressed onto an aluminum substrate and then transferred into the chamber. Then a gas mixture (CO_2/H_2 = 1/2) with a total gas pressure of 10 mTorr was introduced into the chamber. The samples were heated to 673 K with a heating rate of 20 K min^{-1}. The XPS spectra of the Ni 3*p* region with a resolution of 0.1 eV were probed both in the initial state at 300 K and after the temperature was held at 673 K for 30 min. All the binding energies were calibrated by the La $4d_{5/2}$ features with two spin-orbit doublets line located at 101.6 and 104.3 eV.[17] To ensure the quality of the peak fitting, it is assumed that the peak shape and relative intensity ratio (RIR) for Ni^0, Ni^{2+}, and Ni^{3+} are the same in both Ni $3p_{3/2}$ and Ni $3p_{1/2}$. For this purpose, a Shirley background and a combined Lorentzian-Gaussian method are applied; the spin-orbit splitting energy between Ni $3p_{3/2}$ and Ni $3p_{1/2}$ is ~ 2.0 eV and the RIR value of Ni $3p_{3/2}$/Ni $3p_{1/2}$ is controlled at ~ 2.0.[18, 19] The fitting results for all the spectra are presented in Table S3

and S4. The peak at 65.5 eV (A), 67.0 eV (C), and 71.0 eV (E) are assigned to the $3p_{3/2}$ peak of Ni^0, Ni^{2+}, and Ni^{3+}. The peaks at 67.5 eV (B), 69.0 eV (D), and 73.0 eV (F) are assigned to the $3p_{1/2}$ peak of Ni^0, Ni^{2+}, and Ni^{3+}.

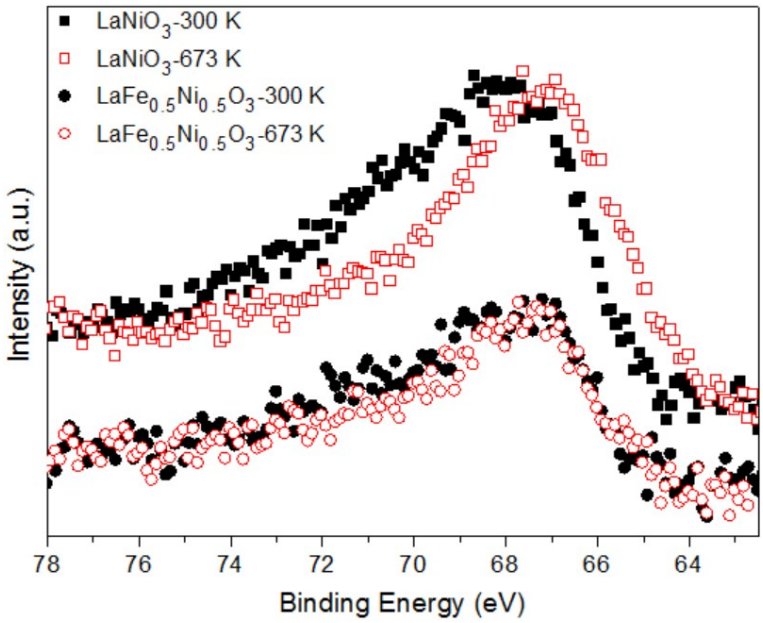

Fig. S8 The *in-situ* AP-XPS spectra of the catalysts.

Table S3. Fitting results of binding energy (BE), relative area (RA), full width at half-maximum (FWHM) and χ^2 from Ni 3*p* XPS spectra of $LaNiO_3$ at 300 K and 673 K.

Peak	$LaNiO_3$-300 K				$LaNiO_3$-673 K			
	BE (eV)	RA (%)	FWHM (eV)	χ^2	BE (eV)	RA (%)	FWHM (eV)	χ^2
A	65.5	0	2.8		65.5	19.4	2.8	
B	67.5	0	2.8		67.5	9.7	2.8	
C	67.0	49.4	2.8	0.2718	66.9	37.6	2.8	0.2800
D	69.0	24.7	2.8		69.0	18.8	2.8	
E	71.0	17.3	3.0		71.0	9.7	3.0	
F	73.0	8.6	3.0		73.0	4.8	3.0	

Table S4. Fitting results of binding energy (BE), relative area (RA), full width at half-maximum (FWHM) and χ^2 from Ni 3p XPS spectra of $LaFe_{0.5}Ni_{0.5}O_3$ at 300 K and 673 K.

Peak	$LaFe_{0.5}Ni_{0.5}O_3$-300 K				$LaFe_{0.5}Ni_{0.5}O_3$-673 K			
	BE (eV)	RA (%)	FWHM (eV)	χ^2	BE (eV)	RA (%)	FWHM (eV)	χ^2
A	65.5	0	2.8	0.5091	65.5	2.0	2.8	0.5241
B	67.5	0	2.8		67.5	1.0	2.8	
C	67.0	46.4	2.8		67.0	48.5	2.8	
D	69.0	23.2	2.8		69.0	24.2	2.8	
E	71.0	20.2	3.0		71.0	16.2	3.0	
F	73.0	10.1	3.0		73.0	8.1	3.0	

9. ***CO hydrogenation***

The CO + H_2 reaction was used to measure the reactivity between CO and H_2 over the surface of the catalysts in the same reactor but equipped with a quadrupole mass spectrometer as the detector. Firstly, 100 mg catalyst (40–60 mesh) was used to perform the CO_2+H_2 reaction as described before at 673 K for 30 min to fully activate the catalyst and then cooled down to 300 K. After that, the catalyst was purged by He and the temperature was ramped to 673 K with a rate of 10 K min^{-1}, simultaneously. After the reactor was cooled down to 300 K again, the gas mixture (CO/H_2/Ar = 5/10/25 ml) was fed into the reactor and the reactor was heated to 673 K with a rate of 10 K min^{-1}. The partial pressures of CO, H_2, CH_4, and CO_2 are functions of temperature.

10. DFT

Density functional theory (DFT) calculations were carried out using the Vienna ab initio simulation package (VASP).[20, 21] The electronic-ion interaction was modeled by the projector augmented wave (PAW) method.[22] The Perdew-Wang-91 (PW91) functional[23] with the generalized gradient approximation was employed to deal with

the electronic exchange and correlation. The kinetic wave cutoff energy is set at 400 eV to describe the electronic wave functions. The Brillouin-zone integration was sampled using a 3×3×1 Monkhorst-Pack k-points grid with a Gaussian smearing of 0.1 eV. Geometries were optimized until the energy was converged to 1.0×10^{-5} eV/atom and the force to 0.01 eV/Å.

The Ni(111) surface was modeled by a four-layer 3×3 super-cell with the coverage of adsorbates of 1/9 ML. For NiO(111) surface, the Ni-terminated surface was selected in the calculations and four bi-layers (four Ni layers and four O layers) were used.[24] The upper two layers together with the adsorbed species are relaxed, whereas the bottom two layers are fixed in their optimized bulk positions. A vacuum layer of 12 Å was added perpendicular to the slab to avoid artificial interactions between the slab and its periodic images. For NiO(111), the Hubbard-U method[25] was applied for the d-electrons of Ni atoms. U = 6.45 eV was used for Ni atoms, which has been successfully used in previous works.[24, 26] The adsorption configurations and binding energies of the CO and HCO species were investigated. As shown in Fig. S9, it is indicated that CO prefers to adsorb at the hollow (fcc and hcp) sites on Ni(111) and NiO(111) surfaces. For CHO, it binds at the bridge site of Ni(111) and NiO(111) surfaces.

The binding energies (*BE*) for all intermediates on metal surfaces are calculated as follows:

$$BE = E_{\text{adsorbate + surface}} - E_{\text{adsorbate}} - E_{\text{surface}} \quad (5)$$

where $E_{\text{adsorbate+surface}}$ is the total energy of the adsorbate together with the surface, $E_{\text{adsorbate}}$ is the total energy of the free adsorbate in the gaseous phase, and E_{surface} is the total energy of the surface.

The activation barrier (E_a) is defined as:

$$E_a = E(\text{TS}) - E(\text{IS}) \quad (6)$$

where, E(IS) and E(TS) refer to the total energies of the initial and transition states, respectively.

Table S5. DFT calculations of binding energies (eV) of CO and CHO on Ni (111) and NiO(111) surfaces.

Surfaces	Species	Configurations	Binding energy (eV)
Ni(111)	CO	fcc, C-bond	-1.93
	CHO	bridge, C-bond	-2.53
NiO(111)	CO	fcc, C-bond	-1.53
	CHO	bridge, C-bond	-3.36

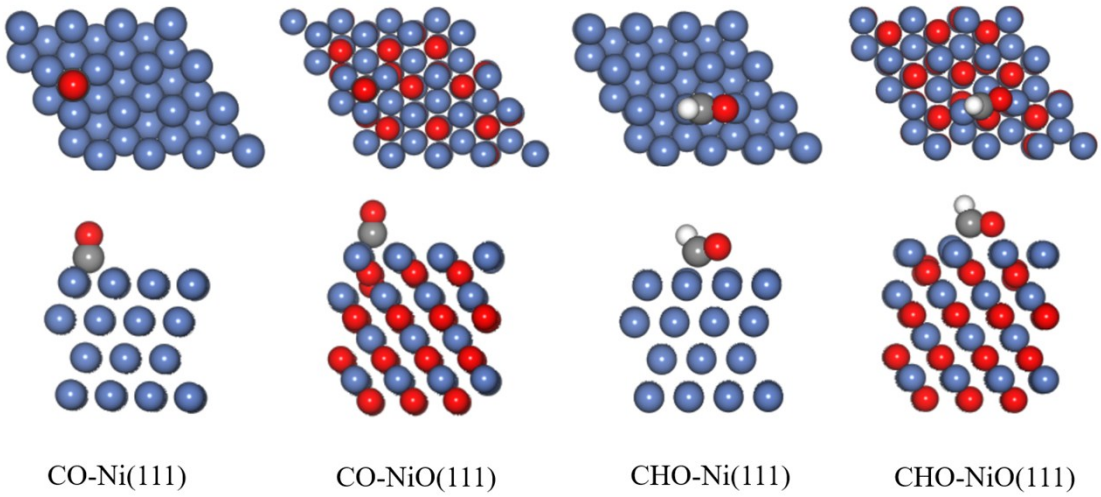

Fig. S9 The adsorption configurations of CO and CHO on Ni(111) and NiO(111) surfaces, Ni: blue, O: red, C: gray, H: white.

11. References

1 L. Zhao, T. Han, H. Wang, L. Zhang and Y. Liu, *Appl. Catal. B: Environ.*, 2016, **187**, 19-29.

2 B. Yan, X. Yang, S. Yao, J. Wan, M. Myint, E. Gomez, Z. Xie, S. Kattel, W. Xu and J. G. Chen, *ACS Catal.*, 2016, **6**, 7283-7292.

3 D. Zubenko, S. Singh and B. A. Rosen, *Appl. Catal. B: Environ.*, 2017, **209**, 711-719.

4 J. L. García-Muñoz, J. Rodríguez-Carvajal, P. Lacorre and J. B. Torrance, *Phys. Rev. B*, 1992, **46**, 4414-4425.

5 M. Gateshki, L. Suescun, S. Kolesnik, J. Mais, K. Świerczek, S. Short and B. Dabrowski, *J. Solid State Chem.*, 2008, **181**, 1833-1839.

6 L. Sangaletti, L. E. Depero, B. Allieri, P. Nunziante and E. Traversa, *J. Eur. Ceram. Soc.*, 2001, **21**, 719-726.

7 S. Royer, D. Duprez, F. Can, X. Courtois, C. Batiot-Dupeyrat, S. Laassiri and H. Alamdari, *Chem. Rev.*, 2014, **114**, 10292-10368.

8 J. A. Alonso, M. J. MartinezLope, J. L. GarciaMunoz and M. T. Fernandez, *Physica B*, 1997, **234**, 18-19.

9 J. Deng, M. Cai, W. Sun, X. Liao, W. Chu and X. S. Zhao, *ChemSusChem*, 2013, **6**, 2061-2065.

10 Y. Luo, X. Wang, Q. Qian and Q. Chen, *Int. J. Hydrogen Energ.*, 2014, **39**, 15836-15843.
11 L. D. Vella, J. A. Villoria, S. Specchia, N. Mota, J. L. G. Fierro and V. Specchia, *Catal. Today*, 2011, **171**, 84-96.
12 S. Singh, D. Zubenko and B. A. Rosen, *ACS Catal.*, 2016, **6**, 4199-4205.
13 M. M. Nair, S. Kaliaguine and F. Kleitz, *ACS Catal.*, 2014, **4**, 3837-3846.
14 P. Steiger, R. Delmelle, D. Foppiano, L. Holzer, A. Heel, M. Nachtegaal, O. Krocher and D. Ferri, *ChemSusChem*, 2017, **10**, 2505-2517.
15 M. Wang, T. Zhao, X. Dong, M. Li and H. Wang, *Appl. Catal. B: Environ.*, 2018, **224**, 214-221.
16 U. Oemar, M. L. Ang, W. F. Hee, K. Hidajat and S. Kawi, *Appl. Catal. B: Environ.*, 2014, **148-149**, 231-242.
17 N. H. Batis, P. Delichere and H. Batis, *Appl. Catal. A: Gen.*, 2005, **282**, 173-180.
18 L. Qiao and X. Bi, *EPL (Europhysics Letters)*, 2011, **93**, 57002.
19 M. Burriel, S. Wilkins, J. P. Hill, M. A. Muñoz-Márquez, H. H. Brongersma, J. A. Kilner, M. P. Ryan and S. J. Skinner, *Energy Environ. Sci.*, 2014, **7**, 311-316.
20 G. Kresse and J. Furthmuller, *Comp. Mater. Sci.*, 1996, **6**, 15-50.
21 G. Kresse and J. Hafner, *Phys. Rev. B*, 1993, **47**, 558-561.
22 G. Kresse and D. Joubert, *Phys. Rev. B*, 1999, **59**, 1758-1775.
23 J. P. Perdew and Y. Wang, *Phys. Rev. B*, 1992, **45**, 13244-13249.
24 W. Zhao, M. Bajdich, S. Carey, A. Vojvodic, J. K. Nørskov and C. T. Campbell, *ACS Catal.*, 2016, **6**, 7377-7384.
25 S. L. Dudarev, G. A. Botton, S. Y. Savrasov, C. J. Humphreys and A. P. Sutton, *Phys. Rev. B*, 1998, **57**, 1505-1509.
26 L. Wang, T. Maxisch and G. Ceder, *Phys. Rev. B*, 2006, **73**, 195107.